Naval Research Laboratory

Washington, DC 20375-5320

NRL/MR/7634--18-9802

Three-Channel Airglow Photometer Data Analysis Methodology

S.A. Budzien
A.W. Stephan
K.F. Dymond
C.M. Brown
P.J. Marquis
A.C. Nicholas

Geospace Science and Technology Branch
Space Science Division

December 11, 2018

REPORT DOCUMENTATION PAGE

Form Approved
OMB No. 0704-0188

1. REPORT DATE *(DD-MM-YYYY)*	**2. REPORT TYPE**	**3. DATES COVERED** *(From - To)*
11-12-2018	Memorandum Report	October 2017 - July 2018

4. TITLE AND SUBTITLE

Three-Channel Airglow Photometer Data Analysis Methodology

5a. CONTRACT NUMBER

5b. GRANT NUMBER

5c. PROGRAM ELEMENT NUMBER

6. AUTHOR(S)

S.A. Budzien, A.W. Stephan, K.F. Dymond, C.M. Brown, P.J. Marquis and A.C. Nicholas

5d. PROJECT NUMBER

5e. TASK NUMBER
62435N

5f. WORK UNIT NUMBER
76-6A74-08

7. PERFORMING ORGANIZATION NAME(S) AND ADDRESS(ES)

Geospace Science and Technology Branch
Naval Research Laboratory
4555 Overlook Avenue, SW
Washington, DC 20375-5344

8. PERFORMING ORGANIZATION REPORT NUMBER

NRL/MR/7634--18-9802

9. SPONSORING / MONITORING AGENCY NAME(S) AND ADDRESS(ES)

Naval Research Laboratory
4555 Overlook Avenue, SW
Washington, DC 20375-5344

10. SPONSOR / MONITOR'S ACRONYM(S)

NRL

11. SPONSOR / MONITOR'S REPORT NUMBER(S)

12. DISTRIBUTION / AVAILABILITY STATEMENT

DISTRIBUTION STATEMENT A: Approved for public release. Distribution is unlimited.

13. SUPPLEMENTARY NOTES

Work Performed under NRL 6.2 Work Unit

14. ABSTRACT

A new class of compact, high-sensitivity three-channel photometers has been developed by NRL for ionospheric remote sensing from CubeSats and other platforms. This report reviews the heritage, details the methodology, and outlines the requirements and assumptions needed to derive ionospheric recombination emission intensities from three-channel photometer data.

15. SUBJECT TERMS

Photometer, Remote Sensing, Airglow, Ionosphere, Nightglow, Aeronomy, Methods

16. SECURITY CLASSIFICATION OF:			**17. LIMITATION OF ABSTRACT**	**18. NUMBER OF PAGES**	**19a. NAME OF RESPONSIBLE PERSON**
a. REPORT	**b. ABSTRACT**	**c. THIS PAGE**			Scott Budzien
Unclassified Unlimited	Unclassified Unlimited	Unclassified Unlimited	Unclassified Unlimited	25	**19b. TELEPHONE NUMBER** *(include area code)* (202) 767-9372

Standard Form 298 (Rev. 8-98)
Prescribed by ANSI Std. Z39.18

This page intentionally left blank.

CONTENTS

1. INTRODUCTION 1
   1.1 Far-ultraviolet Ionospheric Nightglow Sensing 1
   1.2 First Generation Sensor: COSMIC/TIP 1
   1.3 Second Generation Sensor: STP-H5/GROUP-C TIP 3
   1.4 Third Generation Sensor: Tri-TIP 4
   1.5 Three-channel Photometer Methodology 5
2. THREE CHANNEL DATA ANALYSIS 5
   2.1 Signal Contributions per Channel 5
   2.2 Dark Count Rates 6
   2.3 Optical Signal Sensitivity 8
   2.4 FUV Count Rates 10
   2.5 Red-leak Count Rates 12
   2.6 Ionospheric 135.6 nm Brightness 15
3. SUMMARY 17

FIGURES

1. Constellation Observing System for Meteorology, Ionosphere, and Climate (COSMIC) Tiny Ionospheric Photometer (TIP)
2. COSMIC TIP Scattered Light
3. Space Test Program—Houston Payload #5 (STP-H5) GPS Radio Occultation and Ultraviolet Photometry (GROUP-C) TIP
4. Coordinated Ionospheric Reconstruction Cubesat Experiment (CIRCE) Tri-TIP
5. Tri-TIP Optical Paths
6. Strontium Fluoride Absorption Constants versus Temperature
7. Strontium Fluoride and Sapphire Transmittances
8. Ultraviolet Absorption Bands for O_2 and O_3
9. Nitric Oxide Ultraviolet Emission Bands

TABLES

1. Sensitivity Variable Definitions

EXECUTIVE SUMMARY

A new class of compact, high-sensitivity three-channel photometers has been developed by NRL for ionospheric remote sensing from CubeSats and other platforms. This report reviews the heritage, details the methodology, and outlines the requirements and assumptions needed to derive ionospheric recombination emission intensities from three-channel photometer data.

This page intentionally left blank.

THREE-CHANNEL AIRGLOW PHOTOMETER DATA ANALYSIS METHODOLOGY

1. INTRODUCTION

1.1 Far-ultraviolet Ionospheric Nightglow Sensing

During the daytime extreme ultraviolet radiation from the Sun ionizes Earth's neutral atmosphere, building up the F-region ionosphere, which is dominated by O^+ ions. Collisional processes simultaneously produce neutral O atoms through the dominant O^++e recombination process and the slower O^++O^- neutralization processes. After sunset ion production largely ceases, and the recombination and neutralization processes dominate and lead to the decay of the nighttime ionosphere.

An important characteristic of the recombination and neutralization processes is that the neutral O atoms are produced in energetically excited electron states, which then radiatively decay to ground state atoms. This radiative decay generates a number of emission features, including two strong emissions in the far-ultraviolet (FUV) spectral region, the OI 130.4 and OI 135.6 nm multiplets. The 135.6 nm doublet is spin-forbidden and mostly optically thin, whereas the 130.4 nm triplet is an electric dipole allowed transition, and, as such, the photons can be strongly scattered by ambient oxygen atoms. Consequently, the 135.6 emission, directly produced by ions and electrons, provides a means to perform passive remote sensing of the nighttime ionosphere, while the 130.4 nm feature is not as directly useful as an ionospheric diagnostic. Because FUV radiation is completely absorbed by the lower atmosphere, the absence of background emission from the Earth's surface makes the FUV spectral region particularly well-suited to space-based remote sensing techniques.

Space experiments and operational sensors have utilized the 135.6 nm emission to measure the F-region nighttime ion density for decades, employing spectrographs, spectrometers, and narrow-band photometers. All these sensors operate on the principle of spectrally isolating the useful 135.6 nm recombination emission from unwanted 130.4 nm emission and other nightglow features from the neutral atmosphere (such as HI 121.6 nm). These instruments typically employ diffraction gratings or narrowband filters, which can limit their optical efficiency, while spaceflight accommodation constrains their overall size and collecting area. Nearly twenty years ago, NRL introduced the concept for new class of compact, high-sensitivity ionospheric 135.6 nm sensors [Dymond et al., 2000; Dymond et al., 2016]; these sensors subsequently flew on the COSMIC satellites and were refined to provide the basis for the Triple Tiny Ionospheric Photometer (Tri-TIP) sensors [Dymond, et al., 2017], the subject of this report.

1.2 First Generation Sensor: COSMIC/TIP

The *Constellation Observing System for Meteorology, Ionosphere, and Climate,* also known as *Republic of China Satellite 3* (COSMIC/ROCSAT3), is a US-Taiwan constellation of six microsatellites that launched in 2006 to demonstrate the operational utility of global GPS radio occultation data to improve weather forecasts, ionospheric specification, and climate studies. The retrieval of ionospheric density and height from occultation data typically assumes that the ionosphere is spherically symmetric with no horizontal gradients in the vicinity of the occultation. The presence of horizontal ionospheric gradients can introduce errors into the inversion, leading to poor retrieval results. This problem can be addressed by various approaches, which usually entail assimilating additional complementary datasets into the retrieval algorithm. Dymond et al. [2000] determined that photometry could characterize the horizontal ionospheric gradients and supplement GPS occultation results, but that the instrument

Manuscript approved December 11, 2018.

Figure 1. The COSMIC Tiny Ionospheric Photometer sensor assembly measures roughly 16cm×13cm×10cm.

sensitivity should be on the order 100 counts s^{-1} R^{-1} or higher to have sufficient signal-to-noise to impact and improve the GPS retrievals. (One Rayleigh, abbreviated R, is the omnidirectional surface brightness in units of 10^6 photons s^{-1} cm^{-2}. The Rayleigh is a convenient unit for airglow intensity, which typically ranges from ~0.1 R to ~10's kR.) This sensitivity was well beyond the capability of previous FUV sensors that could be accommodated into the COSMIC microsatellites.

The Tiny Ionospheric Photometer (TIP) was developed to meet the need for a high-sensitivity, compact FUV photometer for the nighttime ionosphere (Fig. 1). The optical system was cleverly designed to avoid the low efficiency associated with spectral dispersion and narrowband filters: TIP uses a heated high-pass filter with a favorable short-wavelength cutoff coupled to a high-pass detector with very low quantum efficiency outside the FUV spectral region. Consequently, the theoretical sensitivity for TIP peaked at 600 counts s^{-1} R^{-1} at 135.6 nm, while the unwanted 130.4 nm emission was rejected by a factor of 50 [Budzien et al., 2009]. On-orbit calibration and validation revealed somewhat lower effective sensitivities at ~500 counts s^{-1} R^{-1} [Dymond et al., 2009], but well above the threshold sensitivity requirement. For contrast, the Special Sensor Ultraviolet Limb Imager instruments flying on the *Defense Meteorological Satellite Program* (DMSP) satellites have sensitivities at 135.6 nm of ~0.3 counts s^{-1} R^{-1} [Dymond et al., 2017].

The COSMIC TIP sensors performed well as pathfinders for high-sensitivity, wideband nighttime ionospheric photometry. As might be expected for a low-cost, first-generation instrument, pre-flight tests and on-orbit data revealed some shortcomings of the sensor design and its performance as integrated into the set of microsatellites.

The first problem was red leak, which refers to weak residual sensitivity of the 135.6 nm photometer to detect unwanted longer wavelengths, including visible light ("redder" than ultraviolet). Although the TIP cesium iodide (CsI) photocathode photomultiplier tube (PMT) detector is 3-4 orders of magnitude less sensitive in the mid-ultraviolet and visible region than in the far ultraviolet, the Sun produces about 10^9 times more visible radiation than FUV. The total contamination signal for all wavelengths integrated over the broad passband from 140-750 nm can be comparable to or even exceed the 135.6 nm nightglow signal. Consequently, the ionospheric signal can be contaminated by out-of-band surface signals at night.

The second problem was scattered light, both external to the TIP sensor assembly and within the TIP optical train. The photometer was mounted on the nadir side of the COSMIC microsatellite. Extending below the satellite just outside, but near, the TIP field-of-view was a crossed-dipole antenna for the Tri-Band Beacon experiment [Bernhardt et al., 2000] (Fig. 2, left). The TIP sensor was positioned to peer through an aperture cut in the satellite bus sidewall, but the aluminum honeycomb material left jagged edges around the aperture, which had to be closely matched to the TIP aperture size to minimize the

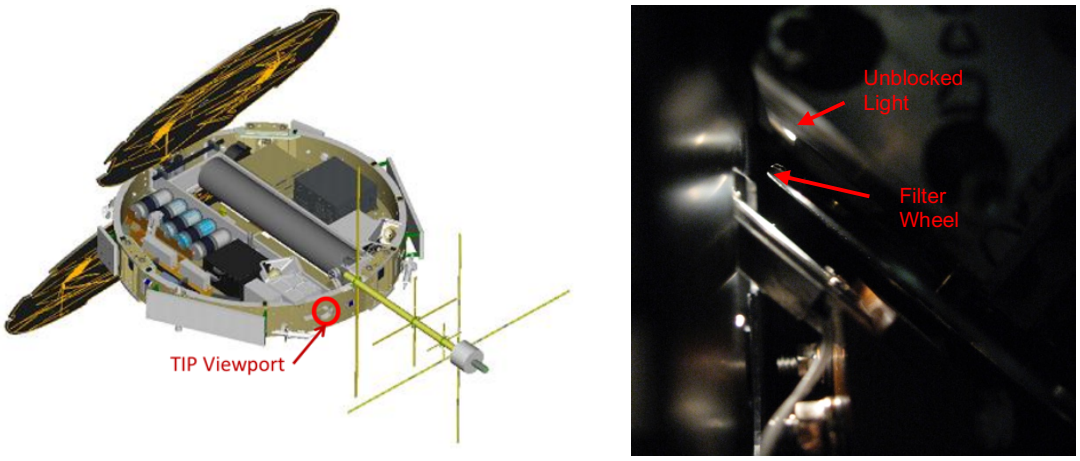

Figure 2. (Left) The bus sidewall and deployed antenna elements near the TIP aperture contribute to scattered light contamination observed near the terminator from sunlight glints. (Right) This laboratory test revealed that visible light unblocked by the filter wheel hit the TIP detector housing near the PMT aperture and scattered inside the instrument.

structural impact of the viewing hole. Finally, within the optical train inside the instrument the filter wheel material was stainless steel and the detector housing surface was iridited aluminum. These materials have poor FUV reflectivity, but significant reflectivity in the visible region (Fig. 2, right). During the mission, when the spacecraft was near the terminator (at orbital altitude, not at the surface) low-angle sunlight scattered from jagged surfaces near the TIP field-of-view and/or the antenna structure into the sensor optical path, and completely overwhelmed the 135.6 signal.

1.3 Second Generation Sensor: STP-H5/GROUP-C TIP

The GPS Radio Occultation and Ultraviolet Photometry Colocated (GROUP-C) experiment aboard the Space Test Program—Houston Payload #5 (STP-H5) launched to the *International Space Station* (ISS) on Feb. 19, 2017. The GROUP-C instrument complement included an upgraded TIP module, which was a refurbished qualification unit from the COSMIC program. Several modifications were made to the TIP optical train to mitigate the scattered light and red-leak problems identified during the COSMIC mission, along a few minor changes for ISS safety compliance and integration with STP-H5 (Fig. 3, left).

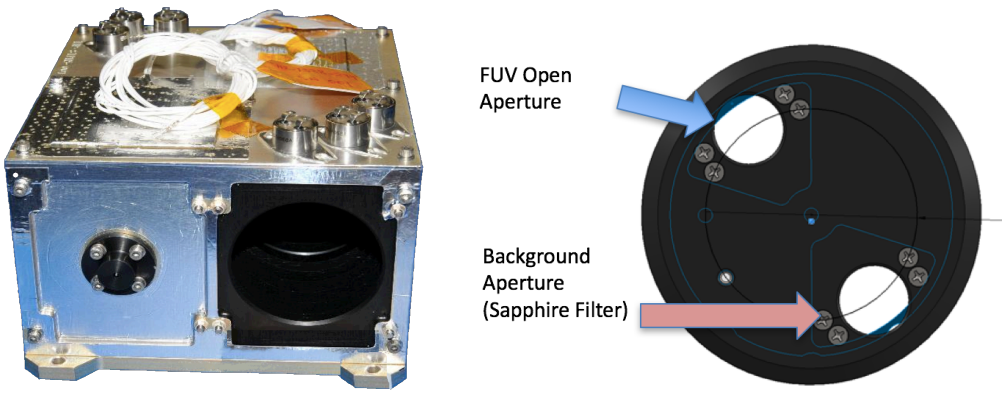

Figure 3. (Left) The refurbished TIP for GROUP-C included optical, electrical, and surface treatment changes for the STP-H5 mission. (Right) The GROUP-C TIP filter wheel is larger in diameter, printed from black Ultem® plastic, and includes both an open aperture and a sapphire filter for red-leak monitoring. The outline of the original, smaller filter wheel is in blue.

The primary change to mitigate the red-leak sensitivity was adding a new filter to the filter wheel. A filter overlay was generated using 3-D printing of vacuum-rated black Ultem® polyetherimide plastic with two filter apertures: one aperture is open to collect FUV signal, and the other is a sapphire window for monitoring red-leak contamination (Fig. 3, right). Sapphire passes radiation with wavelengths greater than 145 nm, which allows monitoring the long-wavelength contamination itself, without the 135.6 nm recombination emission signal. By differencing the measurement through the open aperture (135.6 nm + red leak) and the sapphire filter (red leak only), the O^+ recombination signal can be determined. This measurement scheme was demonstrated using TIP observations from the ISS, in which the filter wheel chopped between the two filters with a 4-second cycle during nightside orbital passes. The method successfully showed that FUV recombination nightglow could be distinguished from red leak contamination. A disadvantage to chopped data collection is that the FUV and background signals are sampled at slightly different times and locations, which affects the accuracy of the FUV measurement and the system's effective spatial resolution. Moreover, the mechanical motion of the direct drive filter wheel was subject to occasional positioning errors by the stepper motor, which caused some data losses.

Other sensor modifications involved reducing the scattered visible light entering the detector by enlarging the filter wheel and blackening surfaces near the detector. The new filter wheel is larger in diameter, black, and tapered to fill as much space as possible. The PMT detector housing was blackened inside and out using an anodized coating. No dipole antenna is located immediately adjacent to the TIP field-of-view, but some ISS structures, such as the large ISS solar panels, can extend below the nadir-viewing instrument as the space station orbits across the terminators. Despite the optical modifications, the GROUP-C TIP unit continues to detect scattered visible light near the beginning and end of each night pass as it crosses the terminator. Finally, the direct drive filter wheel occasionally misaligns the filters relative to the optical axis due to stepper motor and fiducial detection errors, sometimes resulting in reduced throughput, calibration uncertainty, and lower signal-to-noise.

1.4 Third Generation Sensor: Tri-TIP

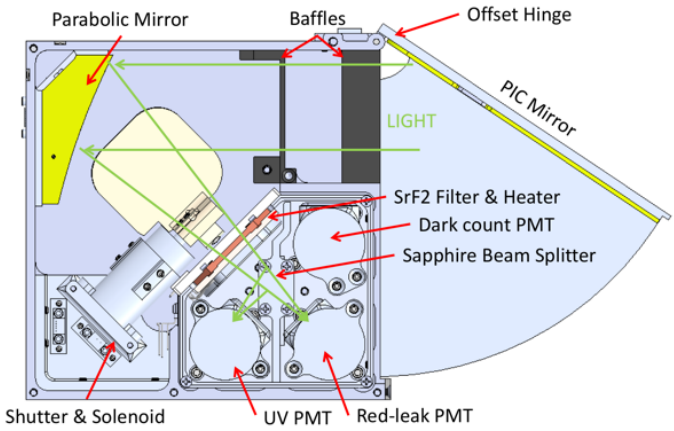

Figure 4. The Tri-TIP three-channel airglow sensor designed for the CIRCE mission. Three detectors continuously monitor UV, red leak, and noise signals, enabled by including a sapphire beam splitter.

The Triple Tiny Ionospheric Photometer (Tri-TIP) [Dymond, et al., 2017] is an ultra-compact three-channel photometer designed for CubeSat accommodation that builds upon the heritage and lessons-learned of the original TIP sensors. The most notable improvements upon the TIP design are that (1) the three-channel unit simultaneously monitors 135.6 nm airglow, red leak, and noise counts continuously; (2) the filter wheel has been replaced with a beam splitter to avoid moving parts and filter misalignments; and (3) the electronics have been miniaturized to fit in 1U form factor. ("1U" refers to a CubeSat module

unit volume of 10 cm×10 cm×10 cm.) The Tri-TIP design uses three separate cesium iodide (CsI) photomultiplier tubes driven by a single high voltage power supply. A sapphire beam splitter separates the incident light into UV+red-leak and red-leak-only beams monitored by two detectors, while a third detector is enclosed and completely darkened to monitor noise counts. A set of four Tri-TIP sensors are being developed for the Coordinated Ionospheric Reconstruction CubeSat Experiment (CIRCE), a US-UK mission to fly lead-trail 6U CubeSats in the 2020 timeframe.

1.5 Three-channel Photometer Methodology

The first and second generation TIP sensors included a single photomultiplier tube and measured each airglow, red leak, or noise signal sequentially. The noise characteristics of individual measurement samples are straightforward and governed primarily by shot noise, i.e. Poisson counting statistics. Deriving an *instantaneous* ionospheric 135.6 nm emission intensity separate from red leak contamination and noise was not possible, either due to a lack of red leak monitoring (COSMIC/TIP) or due to sampling the signals serially, rather than in parallel (GROUP-C TIP).

The purpose of this report is to present the methodology and equations for calculating the instantaneous 135.6 nm signal by differencing the total, red leak, and noise signals of a three-channel photometer. These equations will inform Tri-TIP sensor integration concerning the importance of matching photomultiplier tube detectors with respect to dark count, FUV sensitivity, and red leak sensitivity, and other detector characteristics. They also provide guidance for required ground and on-orbit testing and calibration.

Several additional space environment monitoring applications are being considered for three-channel photometers based upon the Tri-TIP design using various filter and beam splitter combinations. The methodology presented here could be adapted and applied to any Tri-TIP sensor that performs differencing of two optical channels to retrieve environmental data. This report focuses upon the down-looking 135.6 nm photometer for nighttime ionosphere sensing.

2. THREE CHANNEL DATA ANALYSIS

The signal paths of the three channels in the CIRCE Tri-TIP sensors differ significantly. One channel, labelled “dark”, measures the signal from a photomultiplier tube that is completely closed off from the optical path and monitors various forms of noise relevant to all three channels. The main ionospheric measurement channel, designated “uv”, monitors the filtered optical signal from the telescope reflected off the front of the beam splitter. The other channel, called “red”, monitors the filtered optical signal from the telescope transmitted through the beam splitter to exclude 135.6 nm emission and quantify the red leak contamination. In this document, we will use the channel nicknames of the CIRCE mission (“dark”, “red”, and “uv”—always in lower case with quotes) to refer to Tri-TIP channels 1, 2, and 3, respectively. We will use DARK, RED, and UV (always capitalized) to denote the categories of signals that contribute in varying degrees to each of the channels in the equations below, with channel numbers as subscripts or superscripts.

2.1 Signal Contributions per Channel

The circuitry of all three detector channels in Tri-TIP is electrically identical: they are all the same manufacturer and model of PMT, they share a common high voltage supply, and the discriminator and pulse counting circuits are the same. Any differences among the tubes arise from (1) slight variations in noise, sensitivity, and gain due to manufacturing differences and (2) the different optical properties affecting light propagation for each channel. The potential contributions to each channel’s signal are:

- the far-ultraviolet nighttime airglow signals from discrete emission lines in the sensor bandpass producing an event rate R_{UV}^{i} (counts s^{-1}) in Channel *i* is given by

$$R_{UV}^{i} = \sum_{\lambda} B_{UV}(\lambda)\, S_i(\lambda) \tag{1}$$

where $B_{UV}(\lambda)$ is the surface brightness of the airglow of the emission lines in Rayleighs, and $S_i(\lambda)$ is the instrument sensitivity in counts s^{-1} R^{-1} at each wavelength for the channel;

- the integrated count rate from background red leak emission R_{RED} across all wavelengths is given by

$$R_{RED}^{i} = \int_{\lambda} B_{RED}(\lambda)\, S_i(\lambda)\, d\lambda \tag{2}$$

where $S_i(\lambda)$ is the channel sensitivity in counts/sec/Rayleigh with respect to wavelength, and $B_{RED}(\lambda)$ is the background or red-leak spectral intensity in R nm^{-1};

- and the noise rate R_{DARK}^{i} arising from thermal shot noise in the photomultiplier and the integrated events generated by the flux of particle radiation for each channel is

$$R_{DARK}^{i} = N_{PMT}^{i}(T) + \int_{E} F_{CP}(E) A_{CP}^{i}(E)\, dE \tag{3}$$

where $N_{PMT}^{i}(T)$ is the noise rate for each PMT, $F_{CP}(E)$ is spectral flux of charged particle radiation from all sources with respect to particle energy, and $A_{CP}^{i}(E)$ is the effective area for generating a particle noise event with respect to energy.

The expression describing the total count rate R_{TOT}^{i} on any photomultiplier tube channel *i* from all signal sources is therefore

$$R_{TOT}^{i} = R_{UV}^{i} + R_{RED}^{i} + R_{DARK}^{i} \tag{4}$$

$$R_{TOT}^{i} = \sum_{\lambda} B_{UV}(\lambda)\, S_i(\lambda) + \int_{\lambda} B_{RED}(\lambda)\, S_i(\lambda)\, d\lambda + N_{PMT}^{i}(T) + \int_{E} F_{CP}(E) A_{CP}^{i}(E)\, dE \tag{5}$$

We will show that for the 135.6 nm nighttime ionospheric sensors, each of the three channels has an important role in determining one of the signal categories, so the PMT channel "nicknames" in various mission documents carry similar labels. For the purposes of this derivation, the three sensor channels will be labelled numerically by their subscripts/superscripts in equations. The event rates R_{DARK}, R_{RED}, and R_{UV} in the equations do *not* correspond directly to the total count rates on each of the individual sensor channels ("dark", "red", and "uv"), but the underlying signal contributions relevant to all channels in varying degrees.

2.2 Dark Count Rates

Photomultiplier tubes operated in current-mode typically have what is referred to as dark current, which arises from various sources within the PMT itself, in the circuitry, and from external noise sources. Some sources of dark current include thermionic emission from the photocathode and dynode chain, various leakage currents, ionization current from residual gases in the tube, photocurrent from scintillation in the glass, and noise current from particle radiation [Hamamatsu, 2007]. However, many of the effects associated with weak contributions to dark current can be mitigated by operating the PMTs in photon-counting mode, in which only electron cascade events above a threshold amplitude are counted by a pulse amplifier and discriminator circuit.

In pulse counting mode the dark count event rate each channel arises largely from shot noise in the photomultiplier tube from thermionic emission within the detector and the susceptibility of the detector to charged particle noise from cosmic rays, radioactive decay from isotopes in the glass envelope, auroral precipitation, and the South Atlantic Anomaly, a region of intense high-energy particle precipitation that primarily occurs over the South Atlantic Ocean extending westward over much of South America. The shot noise will generally be a characteristic of each individual PMT, as dark noise rates may differ somewhat among and within manufacturing lots. The dark count rate may have a thermal dependence, which can differ according to the work function of the photocathode material [Hamamatsu, 2007]. The charged particle flux spectrum impinging upon the spacecraft $F_{CP}(E)$ is expected to be the same for all photometer channels, but the effective area for charged particles to create a noise event $A^i_{CP}(E)$ on channel i will vary as a function of particle energy E, and may differ due to the PMT location in the spacecraft with respect to shielding and the PMT orientation with respect to the direction of the charged particle precipitation.

$$R^i_{DARK} = N^i_{PMT}(T) + \int_E F_{CP}(E) A^i_{CP}(E)\, dE \tag{6}$$

The CIRCE Tri-TIP photomultiplier tubes are identical Hamamatsu R10825 cesium iodide (CsI) photomultiplier tubes with MgF_2 windows. The tubes are described as "solar blind", because their response to visible light is orders of magnitude less than the FUV quantum efficiency. Once integrated into the sensor, all three detectors are located in a common detector housing behind a strontium fluoride (SrF_2) filter heated to 100 C. Therefore, large differences in temperature among tubes are not expected. How much the PMT housing temperature will vary within an orbit and as a function of orbit beta angle for the CIRCE mission is not known at this time, because the launch vehicle and particular orbit for the mission are not yet defined. For identical tubes the dark noise should vary similarly in response to temperature among the PMTs, and we make the following assumptions about the PMT noise rates among the three channels:

$$N^2_{PMT}(T) = d_2(T) N^1_{PMT}(T) \tag{7}$$

$$N^3_{PMT}(T) = d_3(T) N^1_{PMT}(T) \tag{8}$$

Preflight dark-count testing during thermal cycle or thermal vacuum testing will allow the ratio of PMT noise rates at various temperatures to be characterized for all the channels. How strongly $d_i(T)$ varies with temperature among the tubes is likely to depend upon how much each PMT's noise rate arises from thermionic emission in the photocathode versus other noise sources like ionization current from residual gas and radioactive decay in the glass. Sets of three tubes could potentially be matched to have similar thermal noise characteristics so that the $d_i(T)$ value is a constant; however, other PMT performance characteristics are likely to be much more important for matching tubes into sets.

The detectors are located close together with similar orientations in a detector module, so the shielding from energetic particles by the spacecraft and sensor structure may be roughly similar among tubes. We will assume that responses of each channel to particle noise will be similar (proportional):

$$A^2_{CP}(E) = k_2 A^1_{CP}(E) \tag{9}$$

$$A^3_{CP}(E) = k_3 A^1_{CP}(E) \tag{10}$$

On-orbit dark count testing will allow this assumption to be tested and the constant values k_i to be evaluated as the spacecraft passes in and out of the South Atlantic Anomaly and auroral zones. The increased noise in those regions over and above the ground-based noise rate can be attributed to energetic particle precipitation. Cosmic ray particles, which are much more uniformly distributed but have low flux, may be difficult to distinguish from the other thermal noise measured on the ground.

Finally, since the PMT for Tri-TIP Channel 1 "dark" is completely cut off from the optical path, the sensitivity terms $S^1_{UV}(\lambda)$ and $S^1_{RED}(\lambda)$ in Eq. 5 are identically zero so that

$$R^1_{TOT} = 0 + 0 + R^1_{DARK} = R^1_{DARK} \tag{11}$$

This means that in the special case of Channel 1, the total count rate on the channel R^1_{TOT} can be substituted into the expression for the true dark rate R^1_{DARK} in Eq. 6

$$R^1_{TOT} = N^1_{PMT}(T) + \int_E F_{CP}(E) A^1_{CP}(E)\, dE \tag{12}$$

Combining all of these equations, we may now write expressions for the calculated dark rates for all three photometer channels using a combination of parameters determined through testing and the total count rate observed on Channel 1. We focus first on the dark event rates contributing to Channels 2 and 3 ("red" and "uv") starting with Eq. 6:

$$R^2_{DARK} = N^2_{PMT}(T) + \int_E F_{CP}(E) A^3_{CP}(E)\, dE \tag{13}$$

$$R^3_{DARK} = N^3_{PMT}(T) + \int_E F_{CP}(E) A^3_{CP}(E)\, dE \tag{14}$$

Substituting Eq. 7-10 which relate the noise contributions among channels

$$R^2_{DARK} = d_2(T)\, N^1_{PMT}(T) + \int_E F_{CP}(E) k_2 A^1_{CP}(E)\, dE \tag{15}$$

$$R^3_{DARK} = d_3(T)\, N^1_{PMT}(T) + \int_E F_{CP}(E) k_3 A^1_{CP}(E)\, dE \tag{16}$$

and then by re-arranging Eq. 12, we can solve for the particle noise contribution to Channel 1 noise as the difference between total count rate and the measured dark rate

$$R^2_{DARK} = d_2(T)\, N^1_{PMT}(T) + k_2 \left(R^1_{TOT} - N^1_{PMT}(T) \right) \tag{17}$$

$$R^3_{DARK} = d_3(T)\, N^1_{PMT}(T) + k_3 \left(R^1_{TOT} - N^1_{PMT}(T) \right) \tag{18}$$

Finally, we obtain expressions for the dark rate contributions to Channels 2 and 3, expressed entirely in terms of measured parameters from testing and the observed count rate on Channel 1

$$R^2_{DARK} = [d_2(T) - k_2]\, N^1_{PMT}(T) + k_2 R^1_{TOT} \tag{19}$$

$$R^3_{DARK} = [d_3(T) - k_3]\, N^1_{PMT}(T) + k_3 R^1_{TOT} \tag{20}$$

If we were to make the simplifying assumption that all three tubes exhibited exactly the same noise characteristics and responses to particle radiation, $d_i(T)$ and k_i would be exactly unity. The terms of Eq. 19-20 would simplify to express that Channel 1 exactly reflects the dark noise contribution to the other two channels.

2.3 Optical Signal Sensitivity

The "uv" and "red" detectors (Channels 2 and 3) in the Tri-TIP sensor are exposed to the optical path of the instrument. However, because a beam splitter is used to redirect a portion of the beam, the light path differs slightly between the two channels, leading to different spectral sensitivities. By tracing the

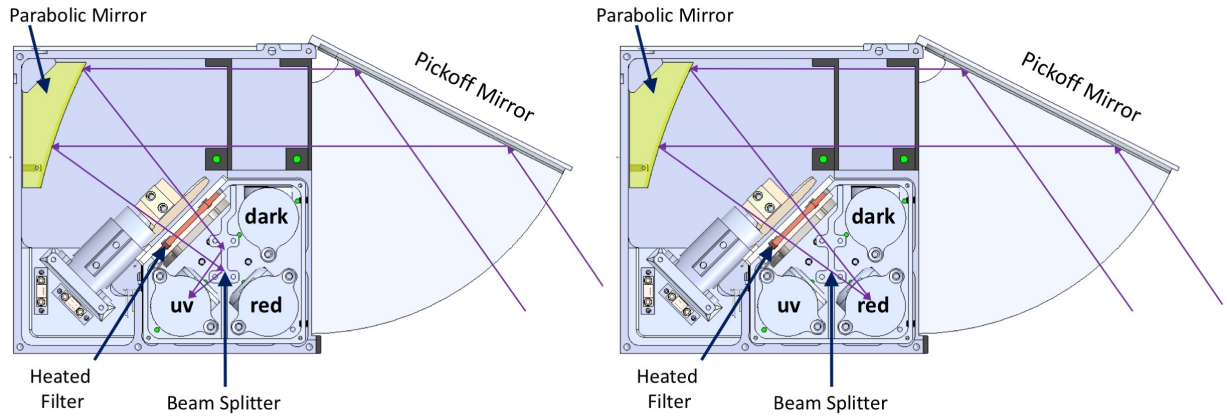

Figure 5. The optical paths for Channels 3 "uv" (left) and 2 "red" (right) differ in their interaction with the beam splitter.

light along the optical path as it interacts with each optical element, we can derive the total sensitivity for these two channels. The aperture area is defined as the parabolic telescope mirror collecting area, and the reflectances of the mirrors and transmittance of the SrF_2 heated filter affect both optical paths equally. However, at the beam splitter, the "uv" beam is reflected from the front while the "red" beam is transmitted through the sapphire substrate. Refraction within the beam splitter introduces a slight difference in focal length for the two light paths, leading to a small difference in solid-angle for the field-of-view.

To compute the sensitivity for the optical channels in counts s^{-1} R^{-1} we obtain slightly different expressions for the Channels 2 "red" and 3 "uv". The variables are defined in Table 1.

$$S_2(\lambda) = \frac{10^6}{4\pi} A_{\text{ap}} R_{\text{pic}}(\lambda) R_{\text{oap}}(\lambda) T_{\text{filt}}(\lambda, \text{T}) T_{\text{bs}}(\lambda) \Omega_2 \eta_2(\lambda) \tag{21}$$

$$S_3(\lambda) = \frac{10^6}{4\pi} A_{\text{ap}} R_{\text{pic}}(\lambda) R_{\text{oap}}(\lambda) T_{\text{filt}}(\lambda, \text{T}) R_{\text{bs}}(\lambda) \Omega_3 \eta_3(\lambda) \tag{22}$$

The terms of these equations can be gathered into convenient expressions that are constant, dependent only upon wavelength, or dependent upon both wavelength and filter temperature. Note that the beam splitter reflectance is included on in the Channel 3 "uv" path, while its transmittance uniquely applies to the Channel 2 "red" path.

$$K_2 \equiv \frac{10^6}{4\pi} A_{\text{ap}} \Omega_2 \tag{23}$$

$$K_3 \equiv \frac{10^6}{4\pi} A_{\text{ap}} \Omega_3 \tag{24}$$

$$\alpha_2(\lambda) \equiv R_{\text{pic}}(\lambda) R_{\text{oap}}(\lambda) T_{\text{bs}}(\lambda) \tag{25}$$

$$\alpha_3(\lambda) \equiv R_{\text{pic}}(\lambda) R_{\text{oap}}(\lambda) R_{\text{bs}}(\lambda) \tag{26}$$

We now rewrite the expressions for the sensitivity of the optical channels (Eq. 21-22) substituting definitions 23-26 to form more compact format expressions that separate the dependencies upon wavelength, temperature, and path. (Quantum efficiency is kept as a separate term for convenience.)

$$S_2(\lambda) = K_2 T_{\text{filt}}(\lambda, \text{T}) \alpha_2(\lambda) \eta_2(\lambda) \tag{26}$$

$$S_3(\lambda) = K_3 T_{\text{filt}}(\lambda, \text{T}) \alpha_3(\lambda) \eta_3(\lambda) \tag{27}$$

Table 1. Sensitivity Variable Definitions

Optical parameter	Channel 2 "red" path	Channel 3 "uv" path	Comments
Aperture	A_{ap}	A_{ap}	(cm^2)
Pick Mirror Reflectance	$R_{pic}(\lambda)$	$R_{pic}(\lambda)$	Acton 1200 MgF_2/Al coating
Off-axis Parabola Reflectance	$R_{oap}(\lambda)$	$R_{oap}(\lambda)$	Acton 1200 MgF_2/Al coating
Heated Filter Transmittance	$T_{filt}(\lambda,T)$	$T_{filt}(\lambda,T)$	SrF_2 temperature-dependent transmittance
Beam Splitter Reflectance	-	$R_{bs}(\lambda)$	Polka dot sapphire beam Splitter
Beam Splitter Transmittance	$T_{bs}(\lambda)$	-	Polka dot sapphire beam Splitter
Focal Length	f_2	f_3	Chan 2/3 focal lengths differ slightly (mm)
Detector Active Area	A_d	A_d	Detector is under-filled (mm^2)
Slit Area	A_s	A_s	Smaller than active area (mm^2) defines FOV
Solid angle	Ω_2	Ω_3	A_s / f^2 (steradians)
Detector Efficiency	$\eta_2(\lambda)$	$\eta_3(\lambda)$	Quantum efficiency

2.4 FUV Count Rates

Tri-TIP is designed as a high-sensitivity FUV photometer for the nighttime ionosphere. The nighttime FUV airglow spectrum is very sparse, with only a few strong features: HI 121.6 nm, OI 130.4 nm, and OI 135.6 nm atomic lines. There is no significant continuum emission in the FUV nightglow spectrum from the thermosphere and ionosphere. Consequently, the integrated signal across the FUV spectral passband reduces to a simple sum over the few discrete emission line features. We use these FUV features to determine R_{UV}^i, the first term in Eq. 5

$$R_{UV}^i = \sum_\lambda B_{UV}(\lambda) S_i(\lambda) = B_{UV}(121.6) S_i(121.6) + B_{UV}(130.4) S_i(130.4) + B_{UV}(135.6) S_i(135.6) \quad (28)$$

The Tri-TIP optical design—particularly the heated SrF_2 filter—ensures that the FUV signal is dominated by 135.6 nm. The short wavelength cutoff of the SrF_2 filter is determined largely by the UV absorption properties of the material, which has strong wavelength dependence; additionally, the effective cutoff wavelength varies linearly with temperature [Tomiki and Miyata, 1969]. The absorption coefficient at 121.6 nm is very large, measured as ~90 cm^{-1} or higher for all temperatures above 78K, corresponding to an intensity reduction of at least 10^8X for a 2-mm thick filter, while the extrapolated absorption coefficients would be much, much higher (Fig. 6). Consequently, the filter transmittance $T_{\text{filt}}(121.6, T)$ can be set to zero, the instrument is completely insensitive to HI 121.6 nm radiation in both optical channels, the 121.6 nm sensitivity from Eq. 26-27 goes to zero, and the 121.6 nm term can be eliminated from Eq. 28.

$$R_{UV}^i = B_{UV}(130.4) S_i(130.4) + B_{UV}(135.6) S_i(135.6) \quad (29)$$

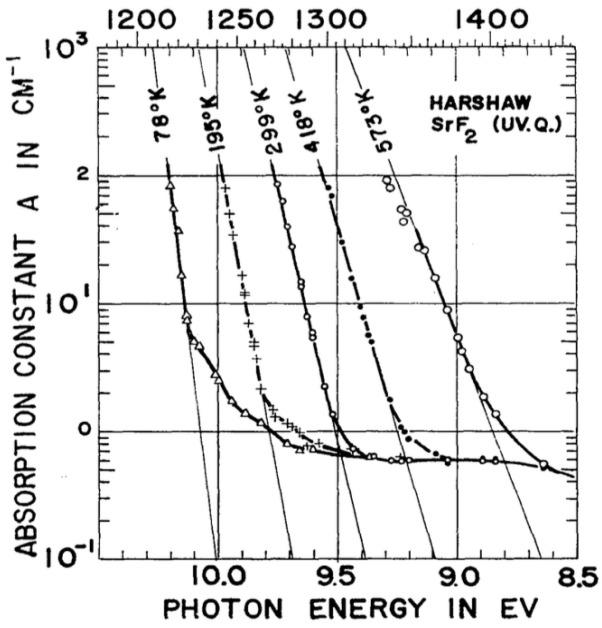

Figure 6. Measured and fitted SrF_2 absorption coefficients for various temperatures excerpted from Tomiki and Miyata [1969, Fig. 4]. Cutoff wavelengths determined from a limiting value of A vary approximately linearly with temperature. For a 2-mm thick SrF_2 filter the highest measured absorption coefficients was ~90 cm^{-1}. The 121.6 nm coefficients are projected to equal or exceed this value for all plotted temperatures (78K and higher) leading to total extinction of any HI 121.6 nm signal.

Heating the SrF_2 filter to 100 C shifts the absorption cutoff to longer wavelengths, and this significantly reduces the transmittance of 130.4 nm relative to the transmittance at 135.6 nm. However, the elimination of 130.4 nm emission by the filter is not nearly as complete as for 121.6 nm, because the SrF_2 absorption constant in the FUV decreases with increasing wavelength. Laboratory measurements of SrF_2 transmittance [Stephan et al., 2017] at NRL indicate that a 100C filter can reduce the 130.4 signal by a factor of ~50X (Fig. 7, left). The implication is that the transmittance term $T_{\text{filt}}(130.4, T)$ in the sensitivity largely eliminates 130.4 nm signal from the beam, but there may be a small residual 130.4 nm contamination in the beam impinging upon the beam splitter. Therefore, we will retain the 130.4 nm term in R_{UV}^{i} to address the potential for 130.4 contamination in the sensor.

The final optical element that can affect the signals from FUV emission lines is the beam splitter. The beam splitter is made from a sapphire window substrate coated with an Acton 1200 Al+MgF_2 polka dot pattern with a 50% filling factor. The front surface of the beam splitter reflects roughly 50% of the beam—including 135.6 nm and residual 130.4 nm—to the Channel 3 "uv" PMT; the other half of the beam passes through the sapphire substrate, where 130.4 and 135.6 nm photons are absorbed out of the beam [Fig. 7, right] before passing to the Channel 2 "red" detector. The short wavelength cutoff for sapphire transmission was measured as 143 nm at 300K [Hunter and Malo, 1969], consistent with recent laboratory measurements [Stephan et al., 2018]. Consequently, absorption characteristics render the sapphire substrate opaque to 130.4 and 135.6 nm radiation, so those terms may be dropped from the Channel 2 ultraviolet signal in Eq. 28.

$$R_{UV}^{2} = 0 \tag{30}$$

$$R_{UV}^{3} = B_{UV}(130.4)S_3(130.4) + B_{UV}(135.6)S_3(135.6) \tag{31}$$

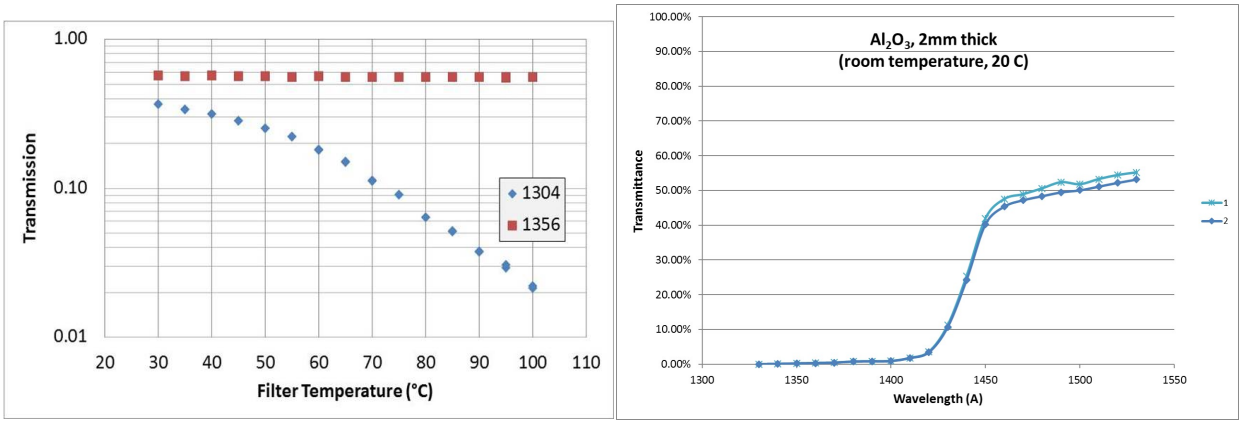

Figure 7. (Left) Measured transmittance at 135.6 nm and 130.4 nm for an SrF_2 filters shows a relatively steady value of 55% at 135.6 nm for all temperatures, while the 130.4 transmittance drops from 35% to 2% from 30C to 100C [Stephan et al., 2018]. (Right) Measured FUV transmittances for two sapphire (Al_2O_3) filters that will be used in the CIRCE beam splitter show that both 130.4 and 135.6 nm signals are strongly absorbed, while longer wavelength radiation is transmitted [Stephan et al., 2018].

2.5 Red-leak Count Rates

Calculating the counts rate expected for the red-leak (or background) contribution to the Channel 2 and 3 signals is challenging, because the origins of the red-leak signal are highly variable in both intensity and spectral characteristics. Red-leak arises from continuum sources (moonlit clouds, scattered twilight) and emission line sources (e.g. Na and Hg city lights, nightglow at UV wavelengths 136-300 nm, and visible 557.7, 630 nm airglow). The optical characteristics of the Tri-TIP optical elements are well-known throughout the visible region, but the performance of the PMTs is not well characterized out to the visible region. Even though the "solar blind" PMT detectors are orders of magnitude less sensitive to visible light than to FUV, the sun—and reflected sunlight from the moon—produce about 10^9X more visible photons across the vast visible passband than FUV photons, resulting in substantial red-leak signal that can exceed the 135.6 nightglow signal.

According to the manufacturer specification [Crystran, 2009], the 2-mm sapphire window transmittance in the region 230 nm to 4 um is fairly uniform at 80-85%, with lower transmittance in the FUV below 230 nm, consistent with our measurements. Likewise, the Acton-1200 MgF_2 coating on the front side of the beam splitter attains a relatively uniform 87-92% reflectance above 230 nm [Acton, 2008]. Consequently, we expect that the light from 230 nm to 4 um passing to the Channel 2 "red" detector should be very representative of (i.e. proportional to) the red-leak light at these wavelengths reflecting from the front of the beam splitter into Channel 3. The integral expression for the red-leak contribution for each channel (Eq. 2) can be split into short- and long-wavelength portions at 230 nm

$$R_{RED}^{i} = \int_{\lambda<230} B_{RED}(\lambda)\, S_i(\lambda)\, d\lambda + \int_{\lambda>230} B_{RED}(\lambda)\, S_i(\lambda)\, d\lambda \tag{32}$$

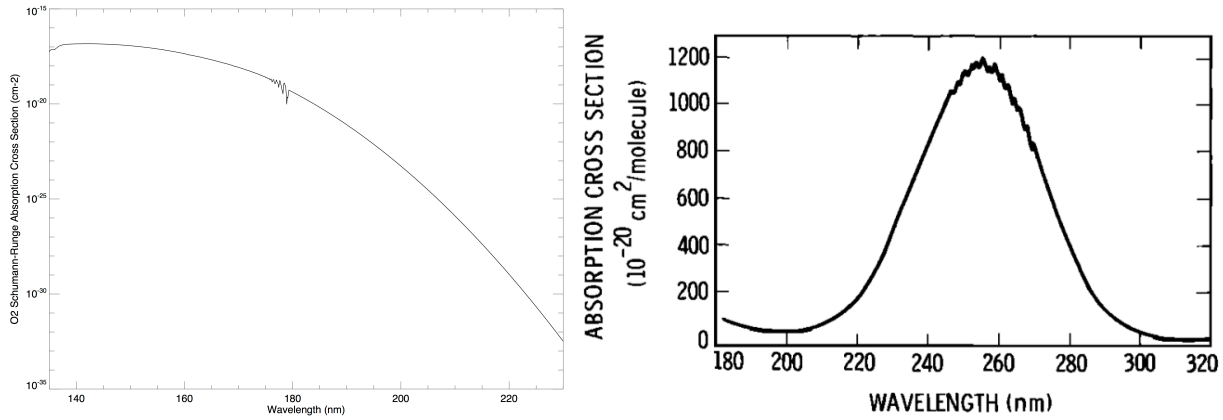

Figure 8. (Left) The Schumann-Runge absorption cross section [Gibson et al., 1983] for 135-230 nm combines with a large O_2 column density to strongly absorb emission originating from the ground at wavelengths 130-203 nm. (Right) The O_3 Hartley band absorption cross section (excerpted from Molina and Molina, 1986) yields strong extinction of ground emissions in the passband 190-290 nm.

The relatively uniform reflectance and transmittance of the beam splitter and their similar minor variation with wavelength longward of 230 nm allows a proportionality constant K_{bs} to be defined such that

$$R_{\mathrm{bs}}(\lambda) = K_{\mathrm{bs}}\, T_{\mathrm{bs}}(\lambda). \tag{33}$$

What about contaminating emission in the region 136-230 nm? Contaminating emission from the ground (such as city lights) must pass through the atmosphere, where absorption by the O_2 Schumann-Runge continuum and ozone Hartley band (Fig. 8) can significantly attenuate the signal. Moreover, in the case of contamination sources relying on reflected light (importantly, moonlit clouds), both the incoming and the outgoing radiation is attenuated while passing through the atmosphere. The NRLMSISE-00 thermosphere model [Picone et al., 2002] estimates a typical O_2 column from the ground to 500 km altitude is 4×10^{24} molecules/cm^{-2}, which leads to extinction optical depths τ_{02} from 10^7 at 135.6 nm to 4 at 203 nm. Nominal O_3 column densities are 8×10^{18} molecules/cm^{-2} (300 Dobson Units [McPeters, et al. 2015]), which yields extinction optical depths τ_{03} of 2.5 at 200 nm to 36 at 230. Thus, the decreasing O_2 absorption from 135 to 230 nm is partially compensated by the increasing O_3 extinction from 190 to 260 nm. The combined extinction from these two species means that no significant ground-based contaminating emission in the 135-240 nm passband is expected our orbiting sensor.

Another potential contribution to red-leak contamination at wavelengths below 230 nm is chemiluminescent emission, particularly the nitric oxide NO delta- and gamma-band nightglow, originating in the lower thermosphere (Fig. 9). The NO delta and gamma bands emit in the 190-270 nm passband [Eastes et al., 1992], and because they are produced above the O_2 and O_3 layers, extinction is low for down-looking viewing geometries. Even so, the sensitivity of the CsI PMT is quite low at 190-270 nm compared to 135.6 nm, so the NO bands are not expected to contribute significantly to the red-leak signal in Channels 2 and 3 relative to the measurement of interest. The spectral responses of beam splitter transmittance and reflectance differ in the 135-230 nm region, so we cannot assume the NO signals in channels 2 and 3 have the same constant ratio independent of the emission spectrum K_{bs} as we assumed for wavelengths greater than 230 nm.

Other upper atmosphere airglow emissions, such as O_2 Herzberg bands, OI 557.7 nm, OI 630 nm are produced above the extinction layers, however, they all occur longward of 230 nm. The uniform spectral responses of the transmittance and reflectance of the beam splitter (Eq. 33) governs these airglow features just like as ground-based emissions below the spacecraft.

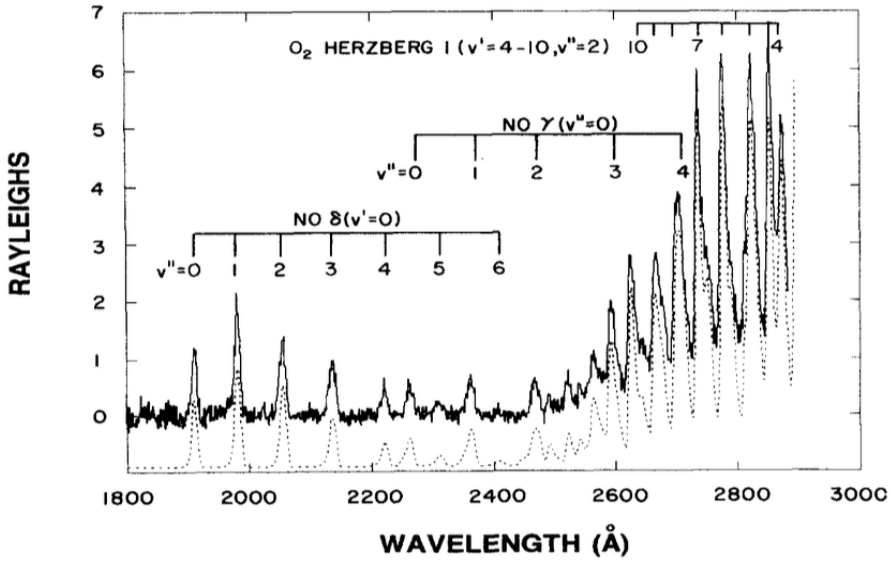

Figure 9. The NO delta- and gamma-band nightglow emission occur in the lower thermosphere, along with O_2 Herzberg bands at longer wavelengths, seen in these down-looking measurements from the S3-4 satellite [from Eastes et al., 1992]. The 190-230 nm passband where the spectral characteristics of the beam splitter transmittance differ from its reflectance are of particular interest, with the potential to introduce error in the red-leak monitor.

Airglow and sensor modeling will be required to estimate the impact of differences between the sapphire filter reflectance and transmittance upon the efficacy and accuracy of Channel 2 as red-leak proxy for Channel 3 in the presence of NO nightglow. To calculate the red-leak contributions, we replace the short wavelength continuous integral with the summation over the discrete NO molecular bands,

$$R^i_{RED} = \int_{\lambda<230} B_{RED}(\lambda)\, S_i(\lambda)\, d\lambda + \int_{\lambda>230} B_{RED}(\lambda)\, S_i(\lambda)\, d\lambda. \tag{32}$$

$$R^i_{RED} = \sum\nolimits_{\lambda_j<230} B_{NO}(\lambda_j)\, S_i(\lambda_j) + \int_{\lambda>230} B_{RED}(\lambda)\, S_i(\lambda)\, d\lambda \tag{35}$$

We inserted the NO emission bands intensities for bands λ_j between190 and 230 nm and assert that there is negligible ground emission in the 135-230 nm passband, especially for down-looking viewing geometries. The NO full-band intensities $B_{NO}(\lambda_j)$ must be expressed as Rayleighs.

We can expand Eq. 35 for the red-leak contributions to Channels 2 and 3 and explicitly include the sensitivity expression for each of the two channels in Eq. 21-22. The similarity of spectral response at long wavelengths (Eq. 33) allowed us to write Eq. 37 in terms of $T_{\rm bs}(\lambda)$

$$\begin{aligned} R^2_{RED} = &\sum\nolimits_{\lambda_j<230} B_{NO}(\lambda_j)\, S_2(\lambda_j) \\ &+ \int_{\lambda>230} B_{RED}(\lambda)\, \frac{10^6}{4\pi}\, A_{\rm ap}\, R_{\rm pic}(\lambda)\, R_{\rm oap}(\lambda)\, T_{\rm filt}(\lambda, {\rm T})\, T_{\rm bs}(\lambda)\, \Omega_2\, \eta_2(\lambda)\, d\lambda \end{aligned} \tag{36}$$

$$\begin{aligned} R^3_{RED} = &\sum\nolimits_{\lambda_j<230} B_{NO}(\lambda_j)\, S_3(\lambda_j) \\ &+ \int_{\lambda>230} B_{RED}(\lambda)\, \frac{10^6}{4\pi}\, A_{\rm ap}\, R_{\rm pic}(\lambda)\, R_{\rm oap}(\lambda)\, T_{\rm filt}(\lambda, {\rm T})\, K_{\rm bs} T_{\rm bs}(\lambda)\, \Omega_3\, \eta_3(\lambda)\, d\lambda \end{aligned} \tag{37}$$

Three variables distinguish the long-wavelength red-leak signal contributions to Channels 2 and 3. The proportionality constant $K_{\rm bs}$ relates beam splitter long wavelength transmittance to reflectance. The solid angle constants $\Omega_{\rm i}$ arise from a focal length difference between the beam reflected from the front of the beam splitter and the portion refracted through the sapphire. The most important terms are the detector efficiencies $\eta_{\rm i}(\lambda)$, because they have a wavelength dependence and because the quantum efficiencies and red-leak response are known to vary among photomultiplier tubes.

These equations describing the red-leak contributions dictate the single most important consideration for matching tubes and successfully performing the signal differencing required for Tri-TIP ionospheric sensing. Because the PMT efficiencies appear within the integral, successful red-leak monitoring requires that for each sensor the "uv" and "red" channels must satisfy

$$\eta_3(\lambda) = K_\eta\, \eta_2(\lambda) \text{ where } \lambda > 230 \text{ nm} \tag{38}$$

where K_η is a constant. This means that the red-leak quantum efficiencies for matched "uv" and "red" PMTs must have a similar (uniformly proportional) spectral response longward of the FUV passband. These measurements of PMT quantum efficiencies can be performed in laboratory facilities in air using broadband light sources and optical filters to characterize $\eta_{\rm i}(\lambda)$ for various segments of 230-800 nm passband. When Eq. 38 is satisfied, we can substitute for $\eta_3(\lambda)$ in the Channel 3 integral of Eq. 37

$$\begin{aligned} R^3_{RED} = &\sum\nolimits_{\lambda_j<230} B_{NO}(\lambda_j)\, S_3(\lambda_j) \\ &+ \int_{\lambda>230} B_{RED}(\lambda)\, \frac{10^6}{4\pi}\, A_{\rm ap}\, R_{\rm pic}(\lambda)\, R_{\rm oap}(\lambda)\, T_{\rm filt}(\lambda, {\rm T})\, K_{\rm bs} T_{\rm bs}(\lambda)\, \Omega_3\, K_\eta\, \eta_2(\lambda)\, d\lambda \end{aligned} \tag{39}$$

and pull out constants from inside the integral

$$\begin{aligned} R^3_{RED} = &\sum\nolimits_{\lambda_j<230} B_{NO}(\lambda_j)\, S_3(\lambda_j) \\ &+ K_{\rm bs}\frac{\Omega_3}{\Omega_2}\, K_\eta \int_{\lambda>230} B_{RED}(\lambda)\, \frac{10^6}{4\pi}\, A_{\rm ap}\, R_{\rm pic}(\lambda)\, R_{\rm oap}(\lambda)\, T_{\rm filt}(\lambda, {\rm T})\, T_{\rm bs}(\lambda)\, \Omega_2\, \eta_2(\lambda)\, d\lambda \end{aligned} \tag{40}$$

The integral in Eq. 40 for Channel 3 is the same as the integral in Eq. 36 for Channel 2. We can eliminate the Channel 3 integral by substituting Channel 2 terms

$$R^3_{RED} = \sum\nolimits_{\lambda_j<230} B_{NO}(\lambda_j)\, S_3(\lambda_j) \; + K_{\rm bs}\frac{\Omega_3}{\Omega_2}\, K_\eta \left[R^2_{RED} - \sum\nolimits_{\lambda_j<230} B_{NO}(\lambda_j)\, S_2(\lambda_j) \right] \tag{41}$$

Gathering like terms and rearranging reveals that the Channel 3 red-leak contribution to event rates has an approximately linear relationship with the Channel 2 red-leak contribution if the NO contamination is small compared to other red-leak sources

$$R^3_{RED} = K_{\rm bs}\frac{\Omega_3}{\Omega_2}\, K_\eta R^2_{RED} + \sum_{\lambda_j<230} B_{NO}(\lambda_j) \left[S_3(\lambda_j) - K_{\rm bs}\frac{\Omega_3}{\Omega_2}\, K_\eta S_2(\lambda_j) \right] \tag{42}$$

2.6 Ionospheric 135.6 nm Brightness

We have derived all the necessary equations required to solve for the 135.6 nm ionospheric airglow signal using the three photometer channels. Start with Eq. 4 for the total signal on Channels 2 and 3

$$R^i_{TOT} = R^i_{UV} + R^i_{RED} + R^i_{DARK} \tag{4}$$

where the term R^i_{TOT} refers to the actual count rate reported in telemetry generated from all emission, red-leak, and noise sources on Channel *i*. Explicitly writing Eq. 4 for each of the three channels and incorporating previous results from Eq. 30 and 31, we obtain the pair of equations

$$R^2_{TOT} = 0 + R^2_{RED} + R^2_{DARK} \tag{43}$$

$$R^3_{TOT} = B_{UV}(130.4)S_3(130.4) + B_{UV}(135.6)S_3(135.6) + R^3_{RED} + R^3_{DARK} \tag{44}$$

Rearranging Equation 44 to solve for the desired 135.6 nm ionospheric brightness in terms of count rates

$$B_{UV}(135.6)S_3(135.6) = R^3_{TOT} - B_{UV}(130.4)S_3(130.4) - R^3_{RED} - R^3_{DARK} \tag{45}$$

and applying Eq. 42 to substitute for the red-leak contribution to Channel 3

$$\begin{aligned} B_{UV}(135.6)S_3(135.6) = {} & R^3_{TOT} - B_{UV}(130.4)S_3(130.4) - K_{\mathrm{bs}}\frac{\Omega_3}{\Omega_2}\,K_\eta R^2_{RED} \\ & - \sum_{\lambda_j<230} B_{NO}(\lambda_j)\left[S_3(\lambda_j) - K_{\mathrm{bs}}\frac{\Omega_3}{\Omega_2}\,K_\eta S_2(\lambda_j)\right] - R^3_{DARK} \end{aligned} \tag{46}$$

We use Eq. 43 to substitute for the R^2_{RED} term

$$\begin{aligned} B_{UV}(135.6)S_3(135.6) = {} & R^3_{TOT} - B_{UV}(130.4)S_3(130.4) - K_{\mathrm{bs}}\frac{\Omega_3}{\Omega_2}\,K_\eta\left(R^2_{TOT} - R^2_{DARK}\right) \\ & - \sum_{\lambda_j<230} B_{NO}(\lambda_j)\left[S_3(\lambda_j) - K_{\mathrm{bs}}\frac{\Omega_3}{\Omega_2}\,K_\eta S_2(\lambda_j)\right] - R^3_{DARK} \end{aligned} \tag{47}$$

and then substitute Eq. 19-20 so that the 135.6 nm brightness can be found in terms of the total count rates on Channels 1-3 and experimentally-determined sensor calibration constants:

$$\begin{aligned} B_{UV}(135.6)S_3(135.6) = {} & R^3_{TOT} - B_{UV}(130.4)S_3(130.4) \\ & - K_{\mathrm{bs}}\frac{\Omega_3}{\Omega_2}\,K_\eta\left\{R^2_{TOT} - \left[[d_2(T) - k_2]\,N^1_{PMT}(T) + k_2 R^1_{TOT}\right]\right\} \\ & - \sum_{\lambda_j<230} B_{NO}(\lambda_j)\left[S_3(\lambda_j) - K_{\mathrm{bs}}\frac{\Omega_3}{\Omega_2}\,K_\eta S_2(\lambda_j)\right] \\ & - \left[[d_3(T) - k_3]\,N^1_{PMT}(T) + k_3 R^1_{TOT}\right] \end{aligned} \tag{48}$$

Finally, the equation can be rewritten so that the first two terms provide a first-order approximation to the 135.6 signal, followed by expressions for minor contaminating emissions and small differences in noise and spectral responsivity. The methodology from determining 135.6 nm O^+ nightglow brightnesses from the 3-channel Tri-TIP sensors is summarized in the following set of equations:

$$
\begin{aligned}
B_{UV}(135.6)S_3(135.6) = {} & R_{TOT}^3 - K_{\mathrm{bs}}\frac{\Omega_3}{\Omega_2}\,K_\eta R_{TOT}^2 - B_{UV}(130.4)S_3(130.4) \\
& - \sum_{\lambda_j<230} B_{NO}(\lambda_j)\left[S_3(\lambda_j) - K_{\mathrm{bs}}\frac{\Omega_3}{\Omega_2}\,K_\eta S_2(\lambda_j)\right] \\
& - \left\{[d_3(T) - k_3] - K_{\mathrm{bs}}\frac{\Omega_3}{\Omega_2}\,K_\eta[d_2(T) - k_2]\right\} N_{PMT}^1(T) \\
& - \left[k_3 - K_{\mathrm{bs}}\frac{\Omega_3}{\Omega_2}\,K_\eta\,k_2\right] R_{TOT}^1
\end{aligned}
\tag{49}
$$

$$K_{\mathrm{bs}} = \left\langle \frac{R_{\mathrm{bs}}(\lambda)}{T_{\mathrm{bs}}(\lambda)} \right\rangle \text{ where } \lambda > 230 \text{ nm} \tag{50}$$

$$K_\eta = \langle \eta_3(\lambda)/\,\eta_2(\lambda) \rangle \text{ where } \lambda > 230 \text{ nm} \tag{51}$$

$$d_2(T) = N_{PMT}^2(T)/N_{PMT}^1(T) \tag{52}$$

$$d_3(T) = N_{PMT}^3(T)/N_{PMT}^1(T) \tag{53}$$

$$k_2 = A_{CP}^2(E)/A_{CP}^1(E) \tag{54}$$

$$k_3 = A_{CP}^3(E)/A_{CP}^1(E) \tag{55}$$

The most important equation for describing the methodology is Eq. 49. Under typical operations with a heated strontium fluoride filter, we would expect its 130.4 term to be about 1/50th of the difference of the first two terms, the NO contribution to be of a comparable small magnitude but variable, and the final noise adjustment terms to be negligible in most cases, outside of high particle noise regions. The importance of Channel 3 as "uv" and Channel 2 as "red" is readily apparent in the dominance of the first two terms; the value of Channel 1 "dark" for noise monitoring manifests in high particle noise conditions; and the other expressions are minor adjustments which can probably be ignored most of the time. Additionally, this set of equations allows us to derive and propagate the uncertainties of the measured 135.6 nm emission brightness from Poisson statistics for each channel, calculated uncertainty in the derived values in Eq. 50-55, measured sensitivity, and modeled contaminating airglow emissions.

3. SUMMARY

The equations for converting the three count rates of a down-looking Tri-TIP sensor into ionospheric nightglow brightness encapsulates the basics for converting raw channel count rates R_{TOT}^1, R_{TOT}^2, and R_{TOT}^3 into environmental measurements. Successfully applying Eq. 49 to derive ionospheric OI 135.6 nm brightnesses rests on the following assumptions and requirements:

- The Tri-TIP sensitivity can be accurately measured at 130.4, 135.6, and 190-230 nm to characterize the airglow lines known to contribute to count rates.
- The amount of 130.4 nm emission can be accurately estimated from models or shown to be negligible.

- $R_{\mathrm{bs}}(\lambda) = K_{\mathrm{bs}}\, T_{\mathrm{bs}}(\lambda)$. The ratio beam splitter reflectance and transmittance are proportional at all wavelengths > 230 nm. This should be verified for the beam splitters in the laboratory prior to integration.
- $\eta_3(\lambda) = K_\eta\, \eta_2(\lambda)$. For all wavelengths > 230 nm the PMTs can be matched for red response such that the Channel 3 "uv" and Channel 3 "red" detectors have spectrally similar (proportional) sensitivity across the passband. This can be measured in the laboratory before matching PMTs for integration.
- $N^{\mathrm{i}}_{PMT}(T) = d_{\mathrm{i}}(T) N^{1}_{PMT}(T)$. The dark count noise of all PMTs can be characterized with respect to temperature and expressed in terms of the thermal noise rates for the Channel 1 "dark" detector. This must be measured on the ground over a range of operating temperatures.
- $A^{\mathrm{i}}_{CP}(E) = k_{\mathrm{i}} A^{1}_{CP}(E)$. The responses of the PMT's to particle radiation noise can be characterized during on-orbit testing and shown to be proportional to the particle noise response of the Channel 1 "dark" tube. This must be measured on-orbit with the shutter closed to calculate the relative noise rates in particle precipitation regions.
- The contributions of NO emissions in the 140-230 nm passband can be estimated from models or shown to be negligible.
- Outside of the auroral zones or SAA region the noise correction term would generally be negligible, as it results from the differencing of vary small count rates.

Other guidelines for selecting and matching sets of triple-channel photometer detectors are to place the highest priority on matching pairs of PMT according to the spectral distribution red-response of the PMTs for wavelengths > 230 nm. Second, to choose the higher 135.6 nm sensitivity PMT of each pair for the "uv" channel. Third, the tubes with lowest optical sensitivity and highest noise rate should be assigned to the "dark" channel.

The equations, assumptions, and requirements outlined in this report will serve as a basis for a complete error analysis of the derived measurements. Understanding measurement uncertainties is critical for performing accurate tomographic reconstructions of the ionosphere, due to a strong dependence of tomographic retrievals upon signal-to-noise characteristics. Future work will be pursued on the topics of limb-viewing Tri-TIP analysis methodology, potential metallic ion multichannel photometer applications, temperature sensing units, and detailed error propagation.

REFERENCES

Acton Optics and Coatings (2008), *Optics & Coatings 120nm – 1064nm*, Sales Brochure, (Acton Optics and Coatings, Acton, MA).

P. Bernhardt, C. Selcher, Sa. Basu, G. Bust, and S. Reising (2000), "10. Atmospheric Studies with the Tri-Band Beacon Instrument on the COSMIC Constellation", *Applications of Constellation Observing System for Meteorology, Ionosphere, and Climate*, pp 291-312 (Springer, New York, NY).

S. Budzien, K. Dymond, C. Coker, and D. Chua (2009), "Tiny Ionospheric Photometers on FORMOSAT-3/COSMIC: On-orbit performance", *Solar Physics and Space Weather Instrumentation III*, *Proc. SPIE,* **7438**, 743813, S. Fineschi, Judy A. Fennelly, ed. (SPIE, Bellingham, WA), doi:10.1117/12.826532.

Crystran Ltd., *Sapphire (Al_2O_3)* (2009)*,* Data Sheet, (Crystran Ltd., Poole, UK).

K.F. Dymond, J. B. Nee, and R. J. Thomas (2000), "9. The Tiny Ionospheric Photometer: An Instrument for Measuring Ionospheric Gradients for the COSMIC Constellation", *Applications of Constellation Observing System for Meteorology, Ionosphere, and Climate*, pp 273-290 (Springer, New York, NY).

K.F. Dymond, S.A. Budzien, C. Coker, and D.H. Chua (2009), "On-orbit calibration of the Tiny Ionospheric Photometer on the COSMIC/FORMOSAT-3 Satellites", ", *Solar Physics and Space Weather Instrumentation III*, *Proc. SPIE,* 7438, 743814, S. Fineschi, Judy A. Fennelly, ed. (SPIE, Bellingham, WA), doi: 10.1117/12.825316.

K. F. Dymond, S. A. Budzien, C. Coker, and D. H. Chua (2016), "The Tiny Ionospheric Photometer (TIP) on the Constellation Observing System for Meteorology, Ionosphere, and Climate (COSMIC/FORMOSAT-3)", J. Geophys. Res. Space Physics, 121, 10,614-10,622, doi:10.1002/2016JA022900.

K. F. Dymond, A. C. Nicholas, S. A. Budzien, C. Coker, A. W. Stephan, and D. H. Chua (2017), "The Special Sensor Ultraviolet Limb Imager instruments", J. Geophys. Res. Space Physics, **122**, 2674-2685, doi: 10.1002/2016JA022763.

K. F. Dymond, A. C. Nicholas, S. A. Budzien, A. W. Stephan, P. Marquis, C. M. Brown, T. Finne, and K. D. Wolfram (2017). "Low-latitude ionospheric research using the CIRCE Mission: instrumentation overview", *Proc. SPIE 10397*, *UV, X-Ray, and Gamma-Ray Space Instrumentation for Astronomy XX*, 1039719.

R. W. Eastes, R. E. Huffman, F. J. Leblanc (1992). "NO and O_2 ultraviolet nightglow and spacecraft glow from the S3-4 satellite", *Planet. Space Sci.*, **40**, 481-493.

S. T. Gibson, H. P. F. Gies, A. J. Blake, D. G. McC oy, and P. J. Rogers (1983). "Temperature dependence in the Schumann-Runge photoabsorption continuum of oxygen", *J. Quant. Spectrosc. Rad. Transfer*, **30**, 385–393.

Hamamatsu Photonics K. K. (2007), *Photomultiplier Tubes: Basics and Operations (Edition 3a)*, (Hamamatsu Corp.—USA, Bridgewater, NJ).

W. R. Hunter and S. A. Malo (1969). "The Temperature Dependence of the Short Wavelength Transmittance Limit of Vacuum Ultraviolet Window Materials—I. Experiment", *J. Phys. Chem. Solids*, **30**, 2739-2745.

R. D. McPeters, S. Frith, and G. J. Labow (2015), "OMI total column ozone: extending the long-term trend record", *Atmos. Meas. Tech*, **8**, 4845-4850, doi: 10.5194/amt-8-4845-2015.

L. T. Molina and M. J. Molina (1986). "Absolute Absorption Cross Sections of Ozone in the 185- to 350-nm Wavelength Range", *J. Geophys. Res.*, **91**, 14501-14508.

J. M. Picone, A. E. Hedin, D. P. Drob, and A. C. Aikin (2002), "NRLMSISE-00 empirical model of the atmosphere: Statistical comparisons and scientific issues", *J. Geophys. Res*., **107**, 1468, doi://10.1029/2002JA009430.

A. W. Stephan, C. M. Brown, K. D. Wolfram, P. Marquis, S. A. Budzien1, K. F. Dymond, and A. C. Nicholas (2018), "Evaluation of UV Optics for Tiny Ionospheric Photometer Sensors for CubeSat Missions", *Proc. SPIE 10769*, *CubeSate and NanoSats for Remote Sensing II*, 10769-32.

T. Tomiki and T. Miyata (1969), "Optical Studies of Alkali Fluorides and Alkaline Earth Fluorides in VUV Region", *J. Phys. Soc. Japan*, **27**, pp. 658-678.